PROCEEDINGS, 42nd Workshop on Geothermal Reservoir Engineering
Stanford University, Stanford, California, February 13-15, 2017
SGP-TR-212

Potential Utilizations of 3D Printed Fracture Network Model

Anna Suzuki[1,2], Kewen, Li[1], Roland N. Horne[1]

[1] 367 Panama St, Stanford, CA 94305, USA

[2] 2-1-1 Katahira, Aoba-ku, Sendai, Miyagi 980-8577, JAPAN

anna3@stanford.edu

Keywords: fracture network, flow experiment, 3D printer, CT scan images

ABSTRACT

Understanding flow mechanisms in fractured media is essential for geoscientific research and geological development industries. This study used 3D printed fracture networks in order to control fracture distributions inside the sample. The accuracy and appropriateness of creating samples by the 3D printer was investigated by using an X-ray CT scanner. The CT scan images suggest that the 3D printer is able to reproduce complex 3D spatial distributions of fracture networks. Flow experiments with the 3D-printed samples were conducted to obtain tracer response curves. This study compared with results from numerical simulations based on a continuum model with the same fracture network. Both experimental and simulation tracer response curves showed truncated power-law distributions. However, there was over two orders difference of travel time because of the oversimplified flow modeling in a continuum model and limitations of the 3D printer technology. This methodology will allow us to validate theoretical models and numerical simulations.

1. INTRODUCTION

Fluid flow within fractured rocks is controlled strongly by fracture distributions. Laboratory experiments give the advantage of evaluating flow properties for the rock samples and improving the understanding of physical mechanisms. However, the fracture distributions are unique in each rock sample, and the results are not duplicable in different samples.

Three-dimensional (3D) printers are useful as rapid prototyping and small scale manufacturing devices. Their applications have become widespread in many research fields. In rock mechanics and mining engineering, Ju et al. (2014) and Jiang et al. (2016) created fracture samples using a 3D printer and investigated the applicability to measuring mechanical properties. Ishutov et al. (2015) and Head and Vanorio (2016) created porous samples to measure petrophysical properties. They created samples by using CT scan images of real rock samples, which can reproduce the same geometries as the specific rock sample at the core scale.

We introduced the 3D printer-based approach to modeling of flow in fracture networks (Suzuki et al., 2016). The tracer responses were obtained by using the fracture networks taking fractal geometry into account. In this study, we present a comparison between a 3D printer-based laboratory experiment and numerical simulations based on a continuum model with the same fracture network model. In previous study, there remained concerns that the wax filling void spaces might not be removed completely after printing. This study examined the post-treatment for printing fractures and observed the cross-sections of the sample by X-ray CT scanning.

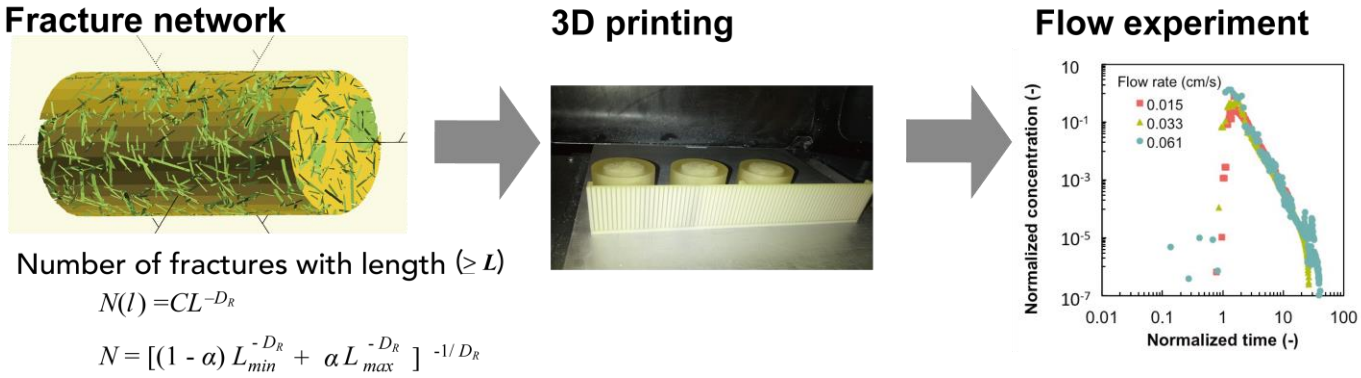

Figure 1: 3D printer-based approach to modeling of flow in fractured media (Suzuki et al., 2016).

2. EXPERIMENTAL SETUP

Specimens of 3D fracture networks with complex geometry require high resolution in 3D printing. We used a 3D printer (VisiJet ® EX200 Plastic Material for 3-D Modeling, 3D Systems) at the Stanford 3-Dimensional Printing Facility, which adopts the multijet modeling (MJM) method. The MJM is a rapid prototyping process that provides a quick turnaround for smooth, high-resolution, hard plastic parts with complex geometries. The official resolution of the printer is 16 micron. The detail of the fracture network can be found in Suzuki et al. (2016). A STL file including the surface geometry of a three-dimensional fracture network was sent to the 3D printer.

UV lamps solidify the UV curable acrylic plastic (VisiJet ® EX200 Plastic Material), creating a fully cured plastic or wax part. The plastic is the base material. The wax filling the void spaces (fractures) needed to be removed from the inside of the sample. After printing, we immersed the samples in an ultrasonic oil bath in which the oil was heated to melt the wax away. The models were submerged in hot water at 60 ^{o}C and shaken for approximately an hour so that the wax melted and floated up through the holes. Because heating and shaking samples did not remove all of wax, Suzuki et al. (2016) used ethanol to dissolve the wax and pumped the ethanol through the sample with a water pump overnight. Instead, the current study used hexane to improve the removal of the remaining wax. Isopropyl alcohol was used to flush the sample to dissolve the hexane.

Assessing the accuracy and appropriateness of creating samples was conducted by comparisons between the cross-sections of the STL file and the cross-sections of the sample created by the 3D printer. The images of cross-sections of the STL file were obtained by a visualization software, Autodesk® Netfabb. In contrast, the cross-sections of the 3D-printed samples were obtained by X-ray CT scanning. The X-ray CT scanning was performed by the ScanXmate-D225RSS270 (Comscantecno Corporation). The parametric values of the CT scanner are summarized in Table 1.The CT scanner provides a three-dimensional distribution of CT values and the cross-sections with a voxel resolution of 35 μm. If the wax remains inside the sample, the fractures would not be detected by the CT scanner.

Table 1: The parameter values of the X-ray CT scanner (the ScanXmate-D225RSS270, Comscantecno Corporation).

Parameter	Parameter Value
Voltage	120 kV
Current	300 mA
Pixel resolution	35.009 μm
CT value for wax (average)	-62
CT value for water	0
CT value for air	-1000

After the wax was removed, we conducted tracer tests using the printed samples. The printed samples were immersed in water under vacuum for full saturation. The water was injected into the samples by hydraulic head difference. The elevation of the water source was set successively to 28, 56, and 114 cm. Time histories of the resistivity and the mass of water at the outlet were measured during the test by using the DE-6000 LCR meter and a digital scale. Once the resistivity had stabilized, two milliliters of salt water were injected as a pulse, representing a tracer test. In a preliminary test, the electrical resistance of the salt water was measured at the outlet using the 100kHz setting of the LCR meter. A power-law representation of concentration between 0.01 % and 5% was obtained and used to convert the measured resistance to concentration. The concentration was normalized by the injected concentration, and time was normalized by the travel time calculated from the flow rate.

3. NUMERICAL FLOW SIMULATION

We generated about 20,000 fractures in a fracture network. Because Discrete Fracture Network (DFN) models were not able to handle the large number of fractures, we conducted flow simulation based on a continuum model (Jing et al., 2000). We divided the calculation area into 126 x 75 x 126 grids ($\Delta x = \Delta y = \Delta z = 0.0003$ [m]) and determined the "equivalent" local permeability on each boundary of two contiguous grid interfaces based on the cubic law. Although the matrix of the 3D printed sample was impermeable, the simulation requires nonzero permeability in the matrix, so this value was set to 10^{-18} m^2. When multiple fractures crossed through a boundary of grid cells, the average values of local permeability were used. We determined the local permeability on surfaces of each grid cell by using the arithmetic area-weighted mean. The local permeability values were used to calculate local flow rates at each grid cell interface in each axis direction by using Darcy's law. In this study, incompressible, single-phase flow was considered. The density of rock and water, the viscosity of water, and the porosity were assumed constant at room temperature. Constant pressure conditions were specified at the points of the inlet and the outlet, and void spaces next to the inlet and the outlet were given high permeability (10^{-5} m^2) and width of 0.001 m, as shown in Figure 2. The boundaries were no-flow conditions. Steady-state flow solutions were solved numerically by relaxation methods using an iterative multigrid algorithm (Jing et al., 2000). A particle-tracking code was used to calculate tracer migration (Suzuki et al., 2015). In total, 50,000 tracer particles were injected as a pulse from the inlet. A tracer particle migrates from a grid cell to its adjacent grid cell until the particle reaches the outlet. The travel direction of tracer particle is determined by a probability that depends on the magnitude of the local flow rates on the six adjacent interfaces of the grid. The frequency of travel time of tracer particles was regarded as a tracer response curve. The simulation parameters are listed in Table 2.

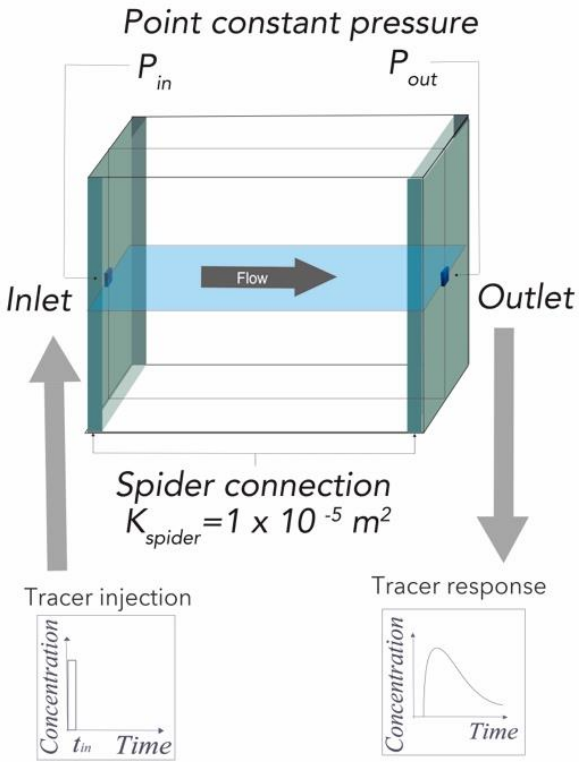

Figure 2: Simulation condition.

Table 2: Numerical properties used in the particle tracking method.

Parameter	Value
Domain [m^3]	$0.042 \times 0.025 \times 0.025$
Number of grid cells [grids]	$126 \times 75 \times 75$
Pressure difference bet`ween the inlet (P_{in}) and the outlet (P_{out}) [Pa]	2800
Viscosity of water [Pa · s] at 23°C	9.321×10^{-4}
Density of water [g/cm^3] at 23°C	0.9975
Number of tracer particles [Particles]	50000

4. RESULTS

4.1 Comparison of cross-sections

The cross-sections of the 3D printed samples and the visualization of the STL files are shown in Figures 3 and 4. Figures 3 and 4 present the results of the sample treated with ethanol and hexane for removing the wax, respectively. The white and light gray parts for the cross-sections of the STL file describe the fractures (void spaces), while the dark gray parts are the plastic. The black parts for the CT scan images are air, while the gray parts describe the material heavier than the air (i.e., plastic and wax). As shown in Figure 3, sparse fractures were observed in the CT scanning images for the sample treated with ethanol. The created fractures were obviously fewer than the fractures in the STL files. The fractures existed only at the right side in the YZ slices (Figure 3(f)). The number of fractures in the XY cross-sections at the inlet (Figure 3(h)) is larger than that at the center (Figure 3(g)). This suggests that the wax remained in the middle of the sample treated with ethanol, that is, removing wax with ethanol was insufficient. On the other hand, the CT scanning images of the sample treating with hexane were similar to the images of the visualization of the STL file (Figure 4). As far as we can see, the hexane is effective in dissolving the wax in the sample, and the 3D printer was able to reproduce complex 3D spatial distributions of fractures. Further research will conduct the quantitative evaluation of the accuracy of creating fractures.

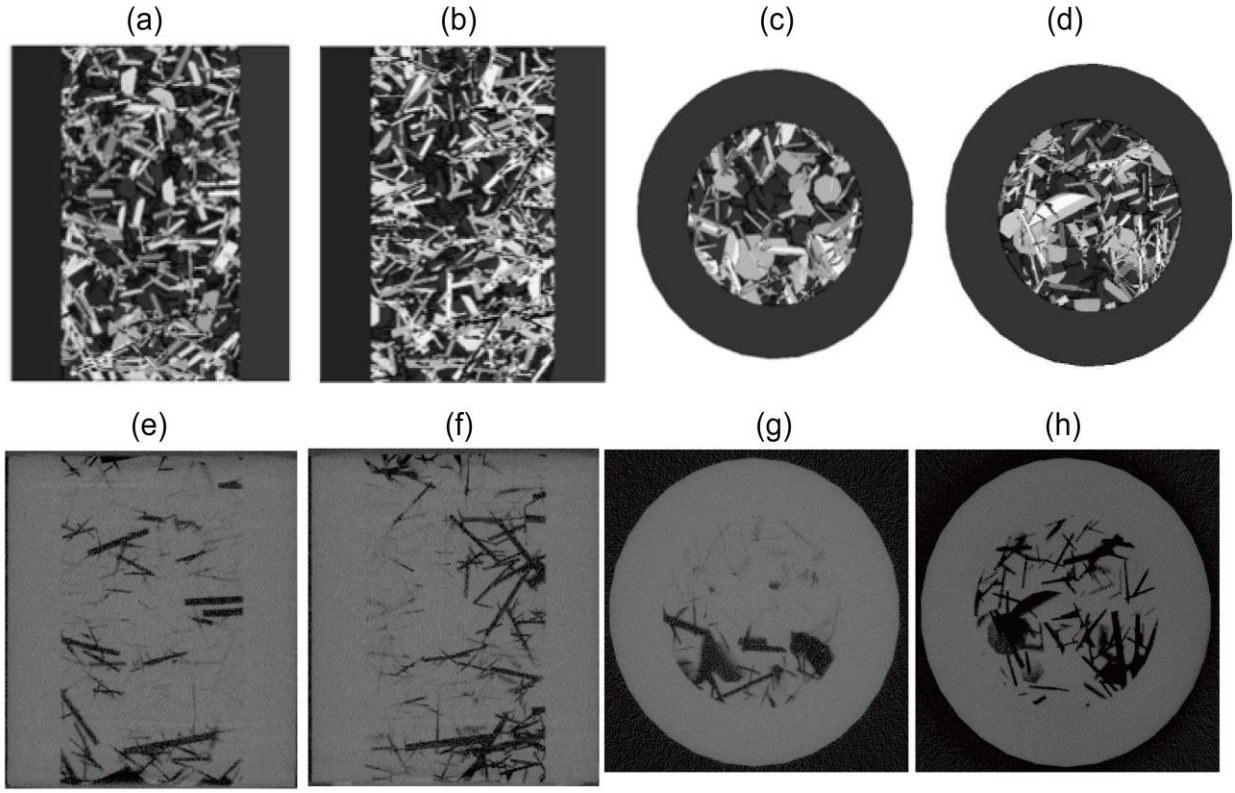

Figure 3: (a)-(d) Cross-sections of the STL file and (e)-(h) cross-sections of the 3D printed sample treated with ethanol: (a)(e) ZX slices at the center, (b)(f) YZ slices at the center, (c)(g) XY slices at the center, (d)(h) XY slices at the inlet.

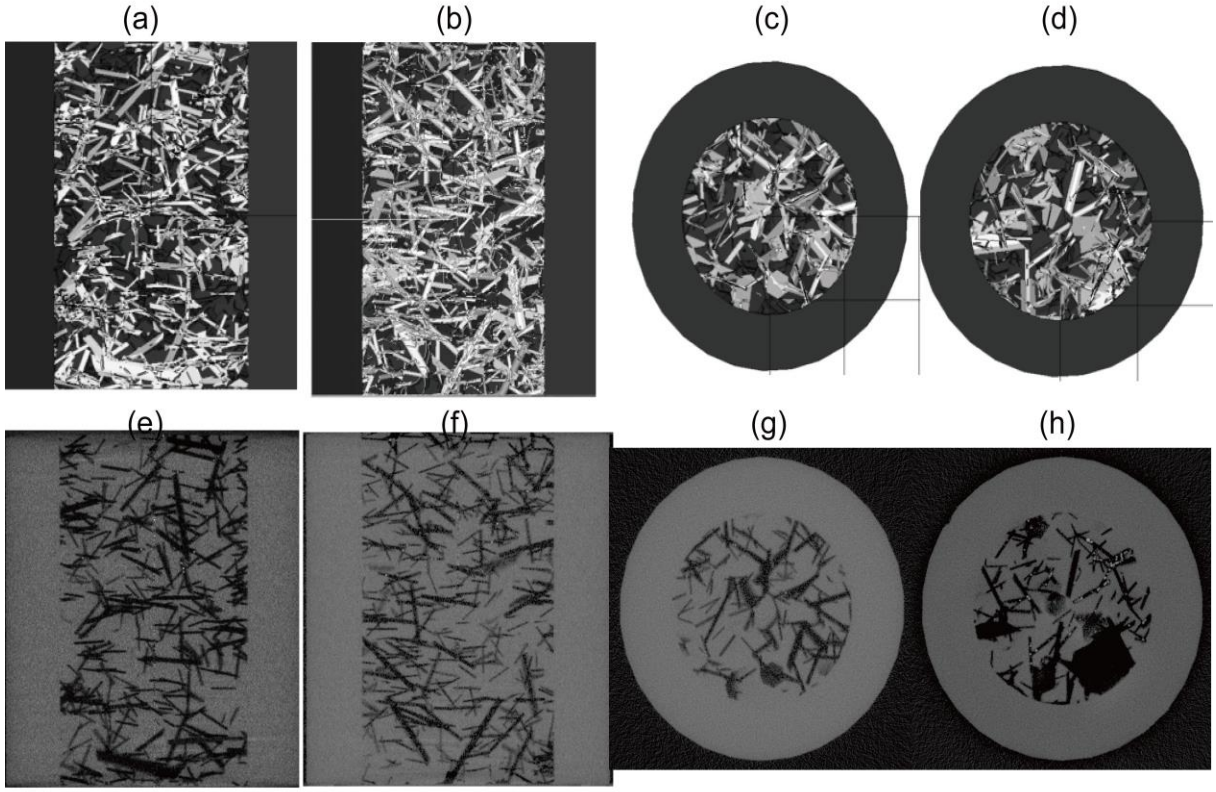

Figure 4: (a)-(d) Cross-sections of the STL file and (e)-(h) cross-sections of the 3D printed sample treated with hexane: (a)(d) ZX slices at the center, (b)(e) YZ slices at the center, (c)(g) XY slices at the center, (d)(h) XY slices at the inlet.

4.2 Comparison of hydraulic properties

We measured the pore volume for the sample treated with hexane by using the displaced volume method. The printed models were immersed in water under vacuum for full saturation. The pore volume was determined to be 5273.18 mm^3. The value from the CT scanner was 5957 mm^3, which was close to the measured value by the displaced volume method.

The experiment was repeated three times with different hydraulic head. Based on Darcy's law, the permeability values were obtained as 2.10×10^{-12}, 2.25×10^{-12}, and 2.03×10^{-12} m^2 for the hydraulic heads of 28, 56, and 114 cm, respectively. This indicates that the permeability was independent of flow rate. Comparison with the simulation results of the permeability is shown in Figure 5. Figure 5 plots the frequency of local permeability and global permeability from the numerical simulation, and the experimental result for the hydraulic heads of 28cm. The global permeability was calculated by using a macroscopic flow rate in Darcy's law. The values of global permeability were determined to be 1.83×10^{-9} m^2 and 8.89×10^{-10} m^2, obtained from the average flow rate (0.138 m/s) and the ratio of the sample length to the peak time of the tracer response (0.6 m/s), respectively. By comparison, the experimental result plotted as the red line was 2.13×10^{-12} m^2, calculated from the flow rate at the outlet. There were over two orders difference between the experimental and the simulation results.

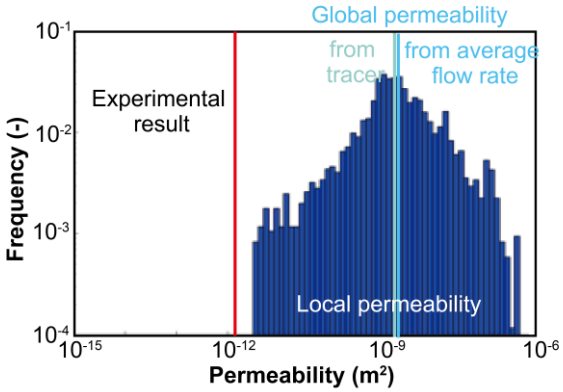

Figure 5: Comparison between the local (dark blue) and the global permeability (light blue) and the experimental result (red).

4.3 Comparison of tracer responses

Figure 8 shows the tracer responses compared between experimental and simulation results. Both experimental and numerical results show power-law declines after the peaks. Previous numerical study (Suzuki et al., 2015) indicated that the long tail resulted from the power-law relationship between the number of fractures and their length. When fractures with a single size were employed instead of power-law relationship, the tracer response fit the conventional advection-dispersion equation without a long tail. In this study, fracture lengths were set in the range from 1.6 mm to 8 mm. The experimental result obtained from the 3D printed sample is consistent with the numerical simulation. The numerical simulation can vary other fracture properties and will provide the relationship with flow behavior. This 3D printer-based study allows us to control fracture properties and obtain the flow pattern in the experiment. This can be useful to validate simulation results.

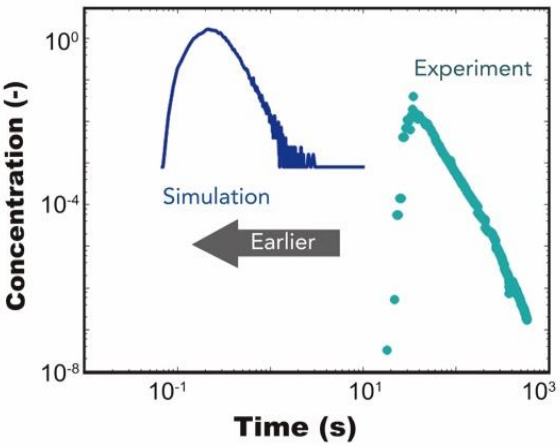

Figure 6: Comparison of tracer responses between experimental and simulation results.

The tracer peak of the experimental results appeared at 24 s, which was delayed from the peak of the numerical results at 0.6 s. The difference between the numerical simulation and the experimental result would be caused by (i) the limitation of creating the samples using the 3D printer and (ii) inappropriate flow modeling.

The 3D printer places each layer upon another to create the 3D products. This leads to nonsmooth fracture surfaces, and the roughness of fracture surface may cause friction. The friction due to the roughness of fracture surface may influence the flow pattern. Witherspoon et al. (1980) proposed Darcy's law with friction parameter, f, accounting for the roughness given by:

$$Q_i = \frac{k_i}{\mu f} \nabla P_i, \tag{1}$$

where Q_i is flow rate, k_i is permeability, μ is water viscosity, and ∇P_i is the pressure difference in i direction. The effect of roughness with different friction parameters is shown in Figure 7(a). The best-fit f was over 100, while the literature value is 1.05-1.65 (Witherspoon et al., 1980). The best-fit value seems to be unconvincingly large.

As far as we can see in Figure 4, the wax could be removed from the sample by using hexane. However, the fracture aperture in the CT scan images seems to be narrower than the visualization of the STL file. This could be caused by the resolution of the 3D printer. We considered the effective aperture given by $\eta' = A\,\eta$ where A is the reduced aperture factor and η is the design value of the aperture generated in the fracture network. Figure 7(b) shows the effect of reduced aperture. If the effective aperture is half of the design aperture (A=0.5), the tracer response was delayed as shown in the green line. If the effective aperture is a quarter of the model aperture (A=0.25), the tracer response was close to the experimental result in the red line. The tracer response with A=0.25 was close to the experimental results. Verification of the reduced aperture factor should be carried out by quantitative comparison between with the CT scan images.

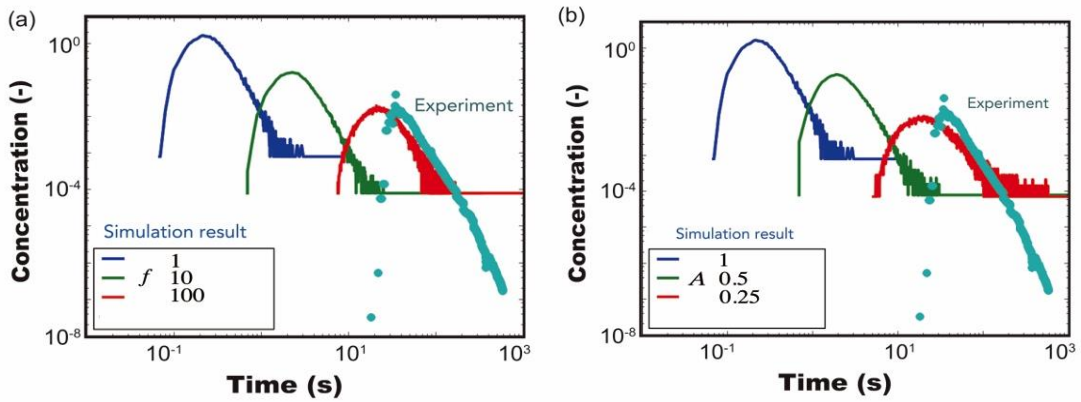

Figure 7: Effects of (a) friction and (b) incomplete fracture aperture.

The numerical simulation used in this study was based on the Darcy's law and the cubic law in the equivalent continuum model. The continuum model-based numerical simulation requires nonzero permeability in the matrix to solve the problem. Even though the permeability distribution has sufficient resolution to account for heterogeneous fracture distributions, the pressure in the matrix needs to be distributed continuously with nonzero value in the simulation. The numerical simulation obliged us to generate grid cells in a cubed Cartesian coordinate system. Diagonal fractures were represented as "staircase" steps, which will lead to discretization errors. In addition, if a fracture is distributed obliquely, the width of the aperture crossing the grid interfaces should be narrower than the aperture in the model. Thus, the current model overestimated the width of the apertures, which needs to be improved in further study.

For the flows in porous media with the Reynolds numbers greater than about 1 to 10, inertial effects cannot be neglected. The Reynolds number, Re, is found as 0.26 with the hydraulic head of 28 cm. Note that $Re = \rho v(2\eta_{max})/\mu$ where η_{max} is the largest fracture aperture (8 mm) and v is the mean velocity given by 0.015 cm/s. Although the value of Re was lower than 1, other simulations using more general equations of fluid dynamics (i.e., Navier-Stokes equations) would provide direct flow behaviors in the fracture networks.

7. CONCLUSIONS

We made a "rock" with a fracture network created using a 3D printer and conducted flow tests. The CT scan images revealed that the 3D printer was able to reproduce complex fracture networks. Comparison between the experimental and the numerical results suggests inaccurate flow modeling and some limitations of the 3D printer technology. Flow experiments using 3D printed models could be groundbreaking for geological studies. If we use 3D printed fracture networks, we can: (i) know all of the fracture configurations, (ii) reproduce the same exact samples for subsequent repeated experiments, and (iii) control the fracture parameters. 3D printers allow us to create fracture geometry of either actual distributions (i.e., CT scan images or outcrop photos) or any type of geometric models (i.e., geometric network or stochastic heterogeneity of petrophysical properties) repeatedly. By using the 3D printed samples, we can conduct flow tests on the same physical configuration multiple times, even if a sample is contaminated or damaged during the experiment. The experimental results can help validate existing flow modeling and numerical methods. We can use the same materials as real rocks

(Fereshtenejad and Song, 2016), which will provide physical, chemical, thermal, mechanical aspects of fluid dynamics in rocks. 3D printer-based flow modeling may be extended to understand transport phenomena in fractured porous media beyond geological fields.

ACKNOWLEDGEMENTS

Many thanks go to Professor Noriaki Watanabe who provided technical support to use the CT scanner for this research. This work was supported by the Japan Society for the Promotion of Science, under JSPS Postdoctoral Fellowships for JSPS Research Fellow (H28-8082), whose support is gratefully acknowledged.

REFERENCES

Fereshtenejad, S., and Song, J.J.: Fundamental study on applicability of powder-based 3D printer for physical modeling in rock mechanics, *Rock Mechanics and Rock Engineering*, **49**, (2016), 2065–2074. http://dx.doi.org/10.1007/s00603-015-0904-x

Head, D., and Vanorio, T.: Effects of changes in rock microstructures on permeability: 3-D printing investigation, *Geophysical Research Letter*, **43**, (2016), 7494–7502. http://dx.doi.org/10.1002/2016GL069334

Ishutov, S., Hasiuk, F.J., Harding, C., and Gray, J.N.: 3D printing sandstone porosity models, *Interpreation*, **3**, (2014), SX49-SX61. http://dx.doi.org/10.1190/INT-2014-0266.1

Jiang, Q., Feng, X., Song, L., Gong, Y., Zheng, H., and Cui, J.: Modeling rock specimens through 3D printing: Tentative experiments and prospects, *Acta Mechanica Sinica*, **32**, (2016), 101–111. http://dx.doi.org/10.1007/s10409-015-0524-4

Jing, Z., Willis-Richards, J., Watanabe, K., and Hashida, T.: A three-dimensional stochastic rock mechanics model of engineered geothermal systems in fractured crystalline rock, *Journal of Geophysical Research*, **105**, B10, (2000), 23663-23679, http://dx.doi.org/10.1029/2000JB900202

Ju, Y., Xie, H., Zheng, Z., Lu, J., Mao, L., Gao, F., and Peng, R.: Visualization of the complex structure and stress field inside rock by means of 3D printing technology, Chinese Science Bulletin, **59**, (2014), 5354–5365. http://dx.doi.org/10.1007/s11434-014-0579-9

Suzuki, A., Niibori, Y., Fomin, S. A., Chugunov, V. A., and Hashida, T.: Fractional derivative-based tracer analysis method for the characterization of mass transport in fractured geothermal reservoirs, *Geothermics*, **53**, (2015), 125–132. http://dx.doi.org/10.1016/j.geothermics.2014.05.003

Suzuki, A., Sawasdee, S., Makita, H., Hashida, T., Li, K., Horne, R.N.: Characterization of 3D printed fracture networks. *Proceedings*, 41st Workshop on Geothermal Reservoir Engineering, Stanford University, Stanford, CA (2016). https://pangea.stanford.edu/ERE/db/GeoConf/papers/SGW/2016/Suzuki1.pdf

Witherspoon, P.A., Wang, J.S.Y., Iwai, K., and Gale, J.E.: Validity of Cubic Law for fluid flow in a deformable rock fracture, *Water Resources Research*, **16**, (1980), 1016–1024. http://dx.doi.org/10.1029/WR016i006p01016